Deconvolution of adaptive optics retinal images

Julian C. Christou

Center for Adaptive Optics, University of California, Santa Cruz, California 95064

Austin Roorda

College of Optometry, University of Houston, Houston, Texas 77204

David R. Williams

Center for Visual Science, University of Rochester, Rochester, New York 14627

Received December 5, 2003; revised manuscript received March 15, 2004; accepted March 23, 2004

We quantitatively demonstrate the improvement to adaptively corrected retinal images by using deconvolution to remove the residual wave-front aberrations. Qualitatively, deconvolution improves the contrast of the adaptive optics images. In this work we demonstrate that quantitative information is also increased by investigation of the improvement to cone classification due to the reduction in confusion of adjacent cones because of the extended wings of the point-spread function. The results show that the error in classification between the L and M cones is reduced by a factor of 2, thereby reducing the number of images required by a factor of 4. © 2004 Optical Society of America

OCIS codes: 100.1830, 100.2980, 100.3190, 170.4470.

1. INTRODUCTION

High-resolution imaging of the living retina has been obtained by using adaptive optics[1] (AO). The wave-front correction is not perfect, however. Although a diffraction-limited core is produced, the residual uncorrected wave front produces a broader underlying halo structure of the point-spread function (PSF) of the AO system that serves to reduce the contrast in the corrected image and to limit quantitative measurements. This effect can be reduced with postprocessing techniques such as deconvolution. Deconvolution has also been proposed as an alternative technique to adaptive wave-front correction through use of the measured wave-front information to generate PSFs to deconvolve the corresponding retinal images[2,3] and also to improve static partially corrected images.[4]

In this paper we investigate the enhanced contrast due to deconvolution of adaptively corrected retinal images by using the improvement in cone classification.[5] Because of the densely packed structure of the cones in the retina, the reflectance of individual cones is contaminated by the light from adjacent cones that is due to the PSF halo structure. This can lead to incorrect individual cone classification and requires many images to permit confident identification of the cone types. The errors in the ability to identify a cone as being either L or M (long or medium wavelength sensitive, respectively) ranged from 2.1% to 5.6% in previously published results.[5,6] To get errors this low, up to 40 images were required. With the original AO ophthalmoscope, collecting this number of good images required many hours of imaging and multiple imaging sessions.

Advances in AO imaging techniques[7] have improved the image quality and have also increased the fraction of acceptable images (some images are still degraded owing to irregular tear film, eye movements, etc.). But the classification of cones still requires a significant time investment. Reducing the time required to identify cones would accelerate the science that can be done and expand the number of patients that can be analyzed with this technique.

Postprocessing of the images is a potential tool that can be used to reduce experiment time as well as improve the quality of the quantitative measurements. It can reduce the number of images that are required for confident identification of cones and does not require any extra subject time. Deconvolution of non-AO retinal images has been demonstrated previously[8] for contrast enhancement of features, but as far as we know, there are no studies of quantitative improvements in the images.

The results presented below demonstrate that deconvolution of AO retinal images not only sharpens AO retinal images but also quantitatively improves the L- and M-cone classification. We apply a blind deconvolution technique, which has been developed for other applications such as AO imaging through the atmosphere, especially astronomy, because of the absence of any residual wavefront measurements for these data. The effect of deconvolution on cone classification is initially investigated for a synthetic data set for which the cone classes are known *a priori*. The results demonstrate the quantitative capability of the algorithm. The technique is then applied to measured AO data of a macaque retina. In both cases the improvement in cone classification with deconvolution is demonstrated.

1084-7529/2004/081393-09$15.00

2. METHODS

A. Spatially Resolved Retinal Densitometry

To identify specific cone subtypes, we combined retinal densitometry[9,10] with high-resolution imaging. Small (1° circular) patches of the retina located approximately 1° from the fovea were imaged with a 4-ms flash of 550-nm light, a wavelength chosen to maximize the absorptance by L- and M-cone photopigments. Individual cones were classified by comparing images taken when the photopigment was fully bleached with those taken when it was either dark adapted or exposed to a light that selectively bleached one photopigment. Images of fully bleached retina were obtained following exposure to 550-nm light (70-nm bandwidth, 37×10^6 td s). Images of dark-adapted retina were taken following 5 min spent in darkness. From these images we created absorptance images, defined as unity minus the ratio of a dark-adapted or selectively bleached image and the corresponding fully bleached image. The absorptance is calculated for each corresponding pixel in the two registered images. If the reflectances are expressed as R_{470}, R_{650}, and R_{full} for the three bleach states, then the absorptances are defined as

$$A_{470} = \left[1 - \left(\frac{R_{470}}{R_{\text{full}}}\right)\right], \qquad A_{650} = \left[1 - \left(\frac{R_{650}}{R_{\text{full}}}\right)\right]. \quad (1)$$

Thus measurements of individual cone reflected intensity will indirectly yield the required absorptances.

The first step in distinguishing S (short-wavelength sensitive) from M and L cones was to generate absorptance images between dark-adapted and fully bleached images in the manner described above. Since the S cones absorb negligibly whereas the M and L cones absorb strongly at the imaging wavelength of 550 nm, the S cones appear as a sparse array of dark cones in the absorptance image, while the M and L cones appear bright. Variations in absolute pigment absorptance, due to, for example, systematic changes in outer segment length, prevented us from identifying all of the S cones using a single absorptance criterion across the entire patch of retina. A subset of cones that did not meet the criterion but were suspected S cones because their absorptance was substantially lower than that of other cones in the neighborhood were also selected as S. Once this sparse population was identified, these cones were removed from the analysis to facilitate the identification of the M and L cones.

To distinguish L and M cones, we took images immediately following each of two bleaching conditions. In the first condition, the dark-adapted retina was exposed to a 650-nm light that selectively bleached the L pigment. In the second condition, the dark-adapted retina was exposed to a 470 nm light that selectively bleached the M pigment. The absorptance image for the 650-nm bleach revealed dark, low-absorptance L cones that had been heavily bleached and bright, highly absorbing M cones spared from bleaching. The absorptance images for the 470-nm bleach showed the opposite arrangement.

Bleaching levels had to be carefully set to maximize the difference in photopigment concentration between the L- and M-cone classes, since overbleaching at any wavelength would leave too little pigment in either type of cone to be useful for identification purposes. Using the wavelength of the bleaching light and our best knowledge of the spectral absorptances of the L and M cones,[11] we calculated their respective bleaching rates. Then we calculated at what bleaching level the maximum difference in concentration would occur and the total concentration of the pigment at that point. Given this concentration, we calculated what the expected reflectance of a contiguous mosaic of cones in the retina should be relative to the dark-adapted and fully bleached reflectances. We set the optimal bleaching levels empirically by regulating the bleach energy until we obtained the desired average retinal reflectance relative to the fully bleached and the dark-adapted retinal reflectances. One caveat is that to calculate the desired reflectance, one needs to know the relative proportions of the L and M cones, which were initially unknown. We initially assumed an L:M ratio of 2:1, and as the experiment progressed we altered the bleaching energy to reflect the actual L:M ratio.

To avoid bleaching the pigment we were trying to measure, we used as little light as possible. As a result, the photon noise in the images was high, and the signal-to-noise ratio was low. To improve the signal-to-noise ratio to a level that made it possible to identify cones reliably, between 20 and 40 images were taken for each bleaching condition. These were later registered by maximizing the cross correlation between pairs of images and were then added together.

The final steps in identifying L and M cones were to plot the relative absorptance of each cone after a 650-nm bleach against the cone's absorptance after a 470-nm bleach. L cones preferentially absorb long-wavelength light and so have low absorptance after a 650-nm bleach. On the other hand, after a 470-nm bleach, L-cone absorptance is relatively high. Because the optical density between cones is variable, the two distributions extend radially from the origin of the absorption plot (see Fig. 1), although self-screening of the photopigments causes the lines to curve somewhat. The length of the line represents the range in optical density of the same pigment. By considering the polar angle θ of each data point from a point near the origin, we can identify the two modes in the scatter plot, which are due to differences in *selective* absorption of L and M cones:

$$\theta = \tan^{-1}\left(\frac{A_{650}}{A_{470}}\right). \quad (2)$$

Cones were identified as L or M by fitting a sum of two Gaussian distributions to the histogram and designating cones on the left and the right side of the intersection as L or M cones, respectively. We estimate how many cones are misidentified by calculating the fraction of each distribution that falls on the wrong side of the dividing criterion.

B. Sources of Error in Cone Identification

There are two main sources of error in the experiment: noise and blur. Ideally, the distribution of L and M cones in the analysis will fall into two modes, which are stretched into lines, owing to variability in the measurable density of photopigment between cones (Fig. 1, top left). When noise is present, the absorption of any given cone may be higher or lower, in a random fashion.

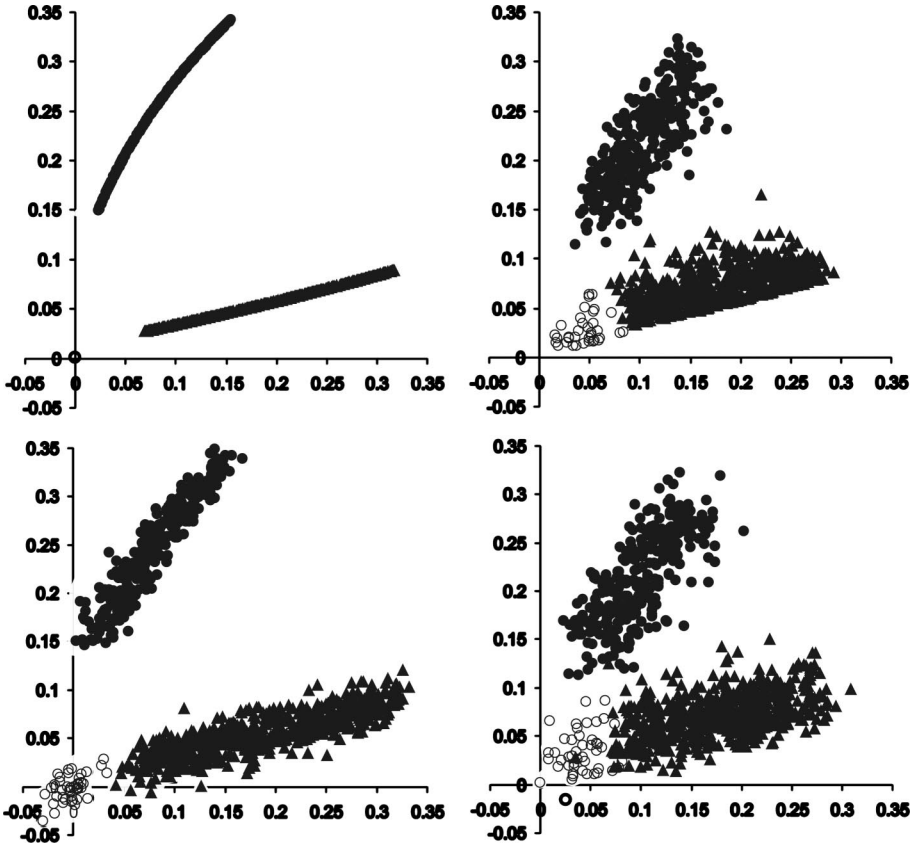

Fig. 1. Simulation showing the effects of noise and blur on the absorptance plots for cones near the fovea. The S, M, and L cones are represented by the symbols ○, ▲, and ●, respectively. Top left, no noise and no blur. The lines are curved owing to self-screening of the photopigments:[12] top right, random noise (3% variance in pixel intensity); bottom left, PSF with 1-arc-min FWHM Gaussian blur; bottom right; noise and blur combined.

Therefore the presence of noise causes the line to broaden about the ideal line.

Blur, on the other hand, has a different effect. When blur is present, each cone will take on the properties of its neighboring cones, including its spectral absorptance. In fact, at the cone spatial frequencies, even after AO, approximately 80% of the light measured from a cone comes from the neighboring cones (i.e., the object is imaged with 20% contrast). Blur has the effect of drawing the two distributions closer together to the extent that when there is enough blur all absorptances appear to fall into a single mode. Figures 1 top right and bottom show a simulation of the separate effects of noise and blur.

Understanding the sources of error govern how the data are to be analyzed. Noise can be reduced by using more pixels to measure the intensity from any given cone. But the effects of blur are best reduced by measuring the reflected intensity as close to the center of the cone as possible (i.e., as far from the adjacent cone as possible). The optimal cone aperture size depends on the magnitudes and relative proportions of noise and blur sources in the images.

C. Deconvolution

Image formation, in the case of PSF invariance, can be simply expressed by the isoplanatic imaging equation, i.e., the convolution of the object with the PSF of the optical system:

$$g(x, y) = f(x, y) * h(x, y), \tag{3}$$

where $g(x, y)$ represents the observed retinal image, $f(x, y)$ the true retinal distribution, $h(x, y)$ the PSF, and $*$ the convolution operator. Given both $g(x, y)$ and $h(x, y)$, the object $f(x, y)$ can be solved for. This inverse problem of deconvolution is not trivial, in particular because the PSF is band limited, i.e., has a cutoff in the spatial-frequency domain due to the finite-sized aperture so that the measured image is also band limited. The true object distribution is not band limited; thus there is the problem of restoring spatial-frequency information not present in the observation. The presence of measurement noise, both Poisson and detector, further complicates the problem. A number of algorithms generally based on maximum-likelihood approaches have been developed to overcome these limitations.[13,14] However, these require the PSF to be well known. Generally, measurements of the PSF are not available during an AO measurement unless a point source is in the field. Although this may be true for astronomical applications, it is not when one is looking at the extended structure of the retina. Thus a more generalized deconvolution technique needs to be applied to these data.

Such a technique is "blind" deconvolution, which permits recovery of the object and the PSF distributions simultaneously from a series of measurements. This is made possible by the use of physical constraints about the

target and knowledge of the imaging system. We have used a multiframe blind deconvolution (MFBD) algorithm that makes use of multiple observations of the same target as a further constraint, thereby reducing the ratio of unknown to known quantities in the problem from 2:1 for a single measurement to $N + 1$:N for N measurements. The solution is further improved if there is a large diversity between the individual PSFs, thus reducing their commonality. A detailed description of the algorithm is given elsewhere[15,16] and is outlined below.

Both object and PSF are constrained to be positive (incoherent imaging), and the PSF is further constrained not to contain any power outside of the diffraction-limited spatial frequency. Multiple observations are solved simultaneously, further constraining the object to be common to all. While MFBD can be shown to produce results without prior knowledge of the target or PSF, it has been found to converge faster and more reliably when such knowledge is available.

The results in this paper rely on quantitative analysis of the deconvolved object distribution. However, it is known from astronomical applications that intensity measurements (photometry) as measured from a deconvolved image can yield larger dynamic ranges in the reconstructed images than in the data; i.e., the fainter sources in the image will appear to be even fainter than they are.[17] For the blind deconvolution algorithm employed here, we have measured the linearity of the deconvolved images and find that it holds for approximately 4–5 stellar magnitudes, i.e., dynamic ranges of 25–100.[18,19] This is within the dynamic range of the retinal images, so linearity can be safely assumed.

D. Synthetic Data

To test the ability of blind deconvolution to improve AO retinal imaging, a set of synthetic observations of a known object was generated. We began with an actual list of cone coordinates and their average intensities (905 cones from a macaque retina) following a full bleach. Each cone's identity (S, M, or L) was randomly assigned, while a fixed L:M ratio and S-cone fraction for the ensemble were preserved. Each cone's photopigment optical density was randomly assigned to lie within a realistic range, which was based on prior experimental observations. The reflected intensity of each cone in the mosaic after full and selective bleaching were computed, with the spectrum and energy of the bleaching lamp, the spectral sensitivity, the bleaching dynamics, and the optical density of the pigments taken into account.

One ideal image was generated for each cone bleaching condition by representing each cone as a disk. Ten blurred images were generated for each bleaching condition by convolving the ideal images with ten different PSFs. The PSFs were computed from actual data on a human eye's wave aberration, which was measured after the AO correction was applied. Each PSF was slightly different because of the variability in the high-order aberrations that is always present, even after AO correction.

E. Actual Cone Images

Real images of the cone mosaic were taken of a macaque monkey with the Rochester Adaptive Optics Ophthalmoscope. The unprocessed results of this particular imaging experiment on the macaque have already been reported.[6] Thirty-six images from each bleaching condition were selected for postprocessing. Each image was slightly different because of the natural variations in aberrations that occurred from frame to frame.

3. RESULTS

A. Synthetic Data

Figure 2 shows sample frames from the synthetic data set. The same set of ten AO PSFs were used for the three bleach cases, hence the similarity of the compensation between the bleach cases. These individual frames show the cones to be clearly identified and that there is flux between the cones due to the uncompensated component of the AO PSF. MFBD was applied to the ten frames simultaneously by using the average measurement as the initial object estimate and a "typical" AO PSF as the initial PSF estimate. We found that when the algorithm was first applied, the object became sharpened but that the PSFs changed very little from their initial estimates. To drive the algorithm to a reasonable solution, the object was held fixed, and ten different PSFs were then deconvolved from the measurements. The code was then restarted by using the object estimate from the first application and the PSFs from the second application and a "relaxed" solution, constraining both to the measurements, was obtained. The deconvolved images are also shown in Fig. 2, showing the sharpening of the images and improved cone separation. Figure 3 compares the reconstructed PSFs for the three bleach cases with the true PSFs. Significant differences can be seen between the AO PSFs, and it is these differences that drive the MFBD algorithm to find a common object solution. The reconstructed PSFs show a strong similarity to the true PSFs, but they are more blurred because of the commonality of structure in the object being selected by the algorithm for the PSF.

The reflectances were measured from both the average and the deconvolved result for all cones in the images. This was done by using an astronomical aperture photometry package, APPHOT in IRAF, that uses circular apertures, centered on the local maxima in the image, as opposed to the rectangular regions used for the prior analysis. Because this is synthetic data with no image-registration problem between the different bleach states, the same cone map was used for all cases. The absorptance was then computed from the reflectance measurements; the results are shown in Fig. 4. The synthetic data were noiseless, so the residual scatter in the distributions was due solely to the blur. The scatter of the measured absorptances in the deconvolved results in Fig. 4 reflect the inherent limitations in measuring the reflectances from the deconvolved images. The linear fits through the L- and M-cone absorptances show standard deviations of 0.012 and 0.020, respectively; i.e., both are $\sim$10%. Considering standard propagation of errors from Eq. (1), this would imply that the reflectances were measured from the deconvolved images with a precision of $\sim$5%.

The different cone classes produce different distributions on the absorptance plot, and although these are evi-

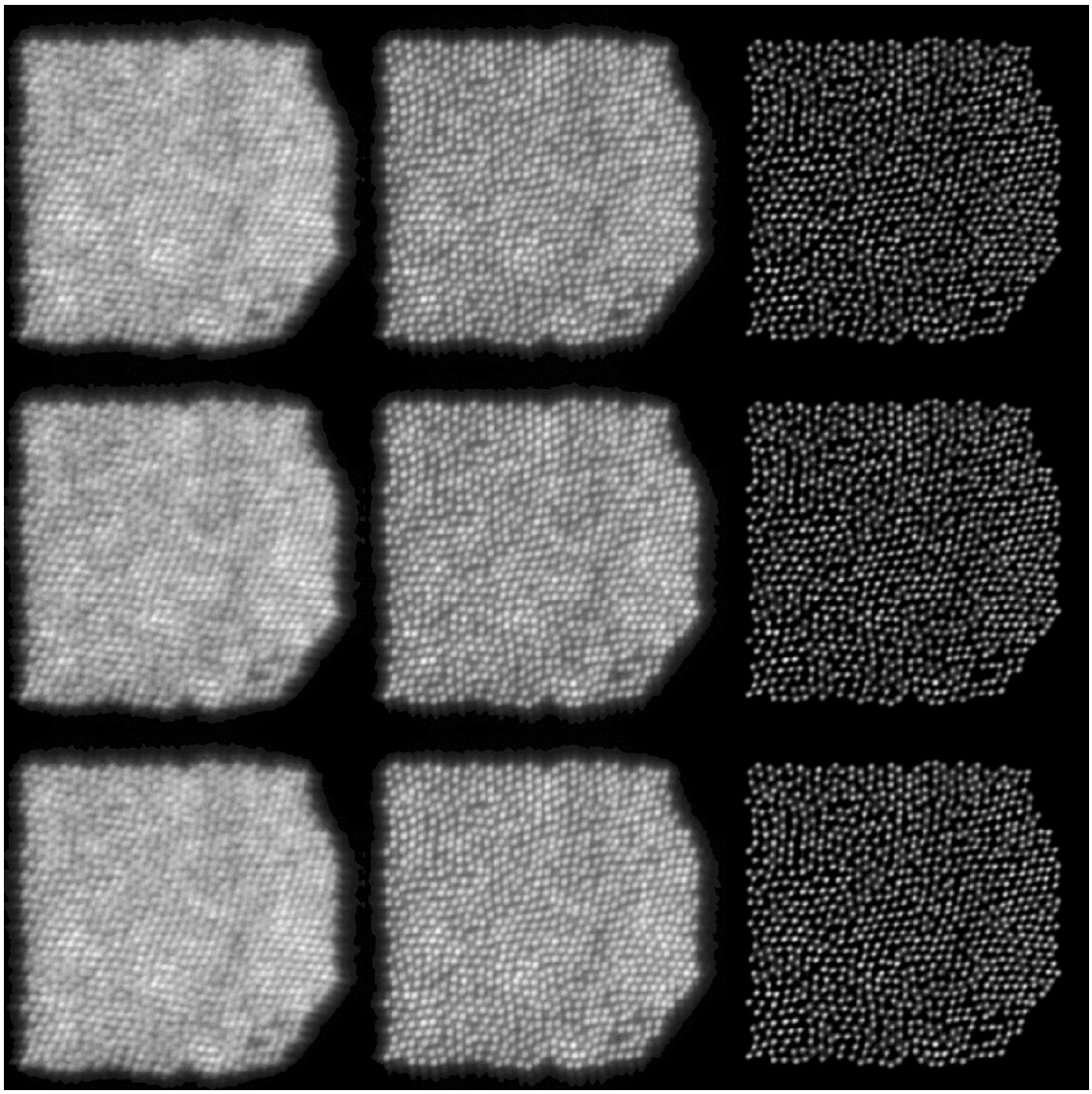

Fig. 2. Left and center columns: Two sample observations (from the set of ten) of the synthetic retinal data set for the three different bleach cases: 470 nm (top), 650 nm (center), and full (bottom). The different reflectances can be seen between the three bleach states as well as the different AO compensation (left and right) between the individual bleach frame pairs. Right column: The corresponding MFBD results. Note that the individual cones are now well isolated with reduction of the overlapping PSFs.

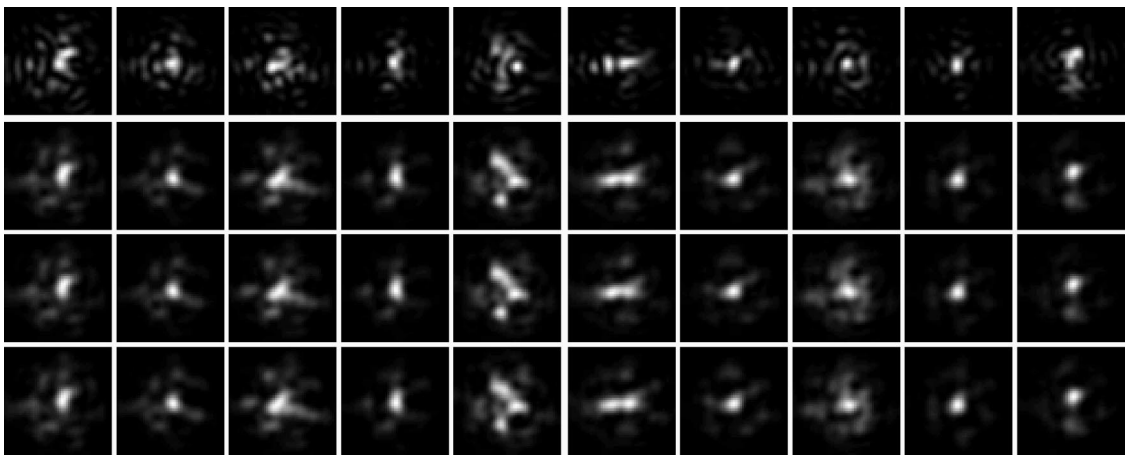

Fig. 3. Original PSFs (top row) compared with the estimate of the PSF from the deconvolution. The rows are deconvolved PSFs from the full, 650, and 470 bleached images, respectively.

dent in the AO compensated result, they are clearly demarcated in the deconvolved result. We note that the absorptance should always be positive because the full bleach reflectance should always be greater than the other two cases. This is no longer true after deconvolution. The nonphysical negative absorptances are due to normalization or the reflectance measurements from the deconvolved data. The distribution of the absorptances rather than their absolute measurement is significant for the cone classification. The cone classification from the deconvolved data showed a 100% correct identification of the cone types, demonstrating that image postprocessing in the form of deconvolution produces significant improvement to quantitative measurements for AO retinal data.

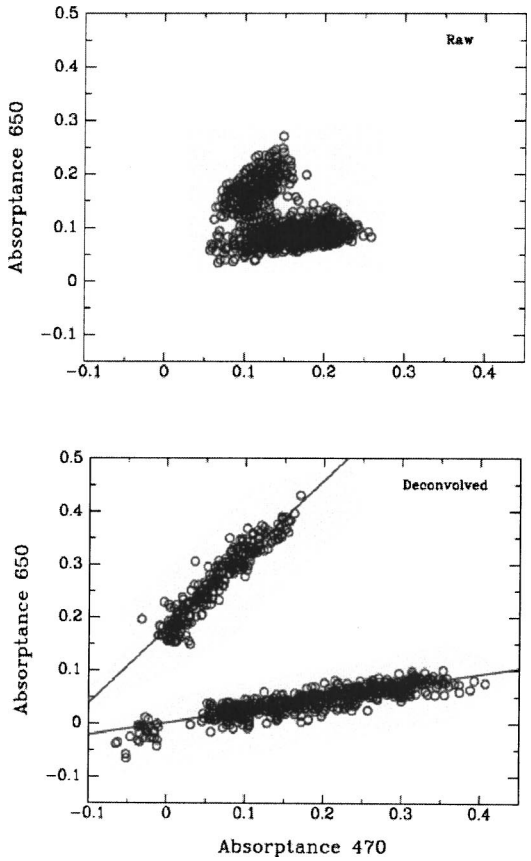

Fig. 4. Cone classification from absorptance measurements for the synthetic images (top) compared with those for the deconvolved images (bottom). These plots illustrate the effectiveness of deconvolution for making quantitative measurements. There is no doubt as to the three different cone classes in the deconvolved case as opposed to the overlapping distributions in the other plot. The solid lines are linear fits to the L and M cones' absorptance distributions.

1. *Real Data*

The algorithm was applied to the three sets of images that were used to classify the L and M cones: 470-nm bleached, 650-nm bleached, and fully bleached images. Each measurement data set comprised 36 frames that had to be corrected for registration errors due to the subject's eye motion. As for the synthetic data, the average frame, shown in Fig. 5, was used as the initial object estimate, but a Gaussian was used as the initial PSF estimate for each frame. The data were reduced in the same way, with the object held fixed after the first set of iterations, and then an improved PSF estimate was calculated. Finally, a relaxed set of object and PSFs were computed. The reconstructed retinal distributions are shown in Fig. 6. These show significantly improved contrast over the nondeconvolved data. Figure 7 compares radial profiles of the high-reflectance cone, in the top left of the full bleach image, before and after deconvolution. The radial profiles of the deconvolved image show an improved contrast by a factor of 6 as well as a reduction in the FWHM of each cone by a factor of almost 3. This shows that the wings of the PSF of an adjacent photoreceptor should contribute less contamination to the intensity of a particular cone. However, does this improve the cone classification?

The above question is investigated by comparing the before and after deconvolution absorptances. The cones selected for the measurement were those used for the previous analysis of this data set.[6] The cone map, comprising 826 cones, is shown in Fig. 8. The S cones, which had been detected by a different analysis, were removed from the list so that we could study how well deconvolution affects the selection of the L and M cones alone. To ensure that the same cones were selected for each of the averaged and deconvolved images, the images were all carefully registered, to within 1 pixel in each direction of the full-bleach deconvolved image.

The absorptance plots for the data are shown in Fig. 9. There are a series of before and after deconvolution plots for five different circular apertures used to measure the reflectances. The deconvolved data clearly distinguish two distinct cone classes. By comparison, the averaged

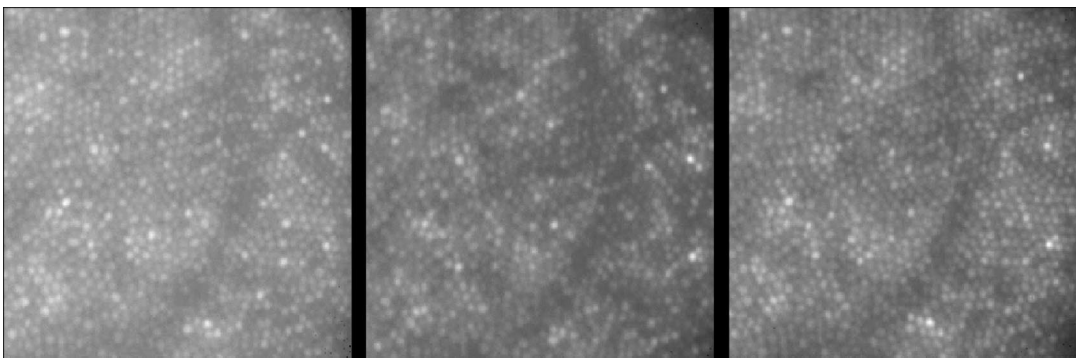

Fig. 5. AO images of a living retina for the three bleach cases: 470 nm, 650 nm, and full bleach (left to right). The individual cones are shown, as are the shadows of blood vessels. Each image is the average of 36 individual measurements.

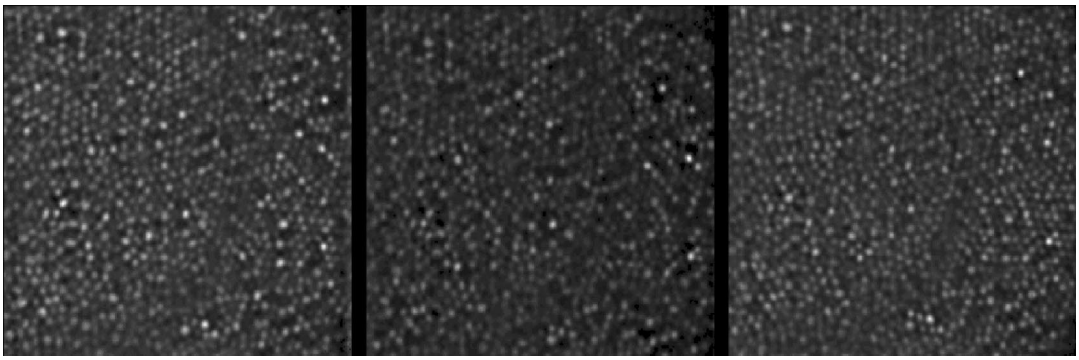

Fig. 6. Deconvolution of the 36 frames making up the averages shown in Figure 5. The contrast is clearly enhanced, signifying reduction of the strength of the PSF wings and with individual cones more clearly identified. Left to right: 470 nm, 650 nm, and full bleach.

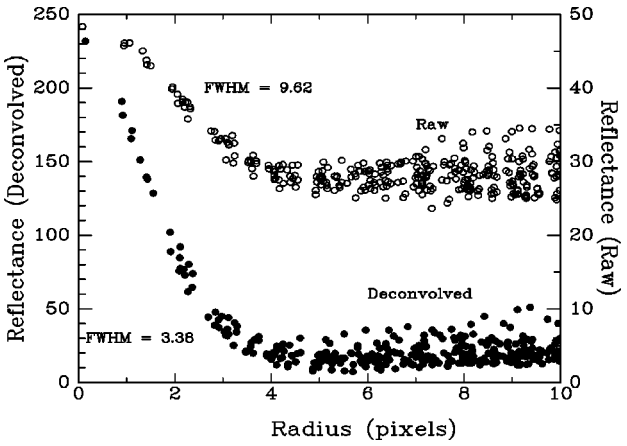

Fig. 7. Radial profiles of a high-reflectance cone before and after deconvolution for the full-bleach image. The contrast of the cone has increased by a factor of ~5–6, and the FWHM has decreased by a factor of ~2.8.

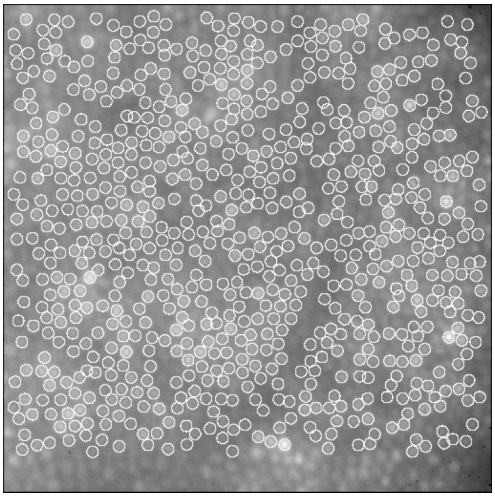

Fig. 8. L and M cones used for the radiometric analysis superimposed over the full-bleach deconvolved image. The circles have a radius of 3 pixels.

frames show substantial confusion between the two populations. As the aperture size increases, the confusion between the two distributions increases, although they can still be seen clearly in the deconvolved case. This demonstrates the effect of the adjacent cones on the measurements. For circular apertures of radii less than 3 pixels, it can be seen that the two distributions remain distinct in the deconvolved results. The average radial separation between the cones is ~7–8 pixels, so the contribution from adjacent cones is small for aperture radii of 3 pixels or less for a 3–4-pixel FWHM peak. However, for the nondeconvolved case, the separation is of the order of the FWHM, so there is significant contamination even at small apertures. The use of larger apertures has an important effect on signal-to-noise ratio, as it reduces the contribution of noise in the cone reflectance measurements.

Unlike with the synthetic data, the distinction among the different cone types is not as apparent, especially in the compensated but nondeconvolved data. Here the two-absorptance plot appears to show a scatterplot without any clear distinction. However, for the deconvolved data there are two distinct distributions, although there is clearly a significant amount of residual scatter. There are two possible reasons for this. The first is unconstrained cone selection, where some cones are still located in the blood vessel shadow, which can change from one exposure to another and also from one bleach case to another. The second reason may well be the changes in the cone reflectance over time.[20] For the 36-frame data set, collected over a period of ~8 h, some cones showed fluctuations of 100% or greater for a single bleach case.

2. Error Analysis

From each of the scatterplots in Fig. 9, we classified the cone types and determined the magnitude of the cone assignment error (i.e., the percentage of cones that are incorrectly identified). All cones in the scatterplot were plotted in a histogram of cone number as a function of angle from a specified origin (Fig. 10). The origin was selected to maximize the separation between the two modes in the plot, as indicated by the presence of a bimodal histogram.

A sum of two Gaussians (6 degrees of freedom; position, height, and sigma for each Gaussian) was fitted to the data. The cones were labeled L or M, according to which side of the intersection of the two Gaussian functions they fell on. The error was computed as the fraction of area of overlap between the two Gaussians divided by their total area. The error, expressed as the percentage of misiden-

tified cones, is plotted in Fig. 11. The plot shows clearly that deconvolution reduces the error in the identification of the L and M cones in the macaque mosaic. Furthermore, it shows that the optimal cone aperture size for measuring intensity is larger for deconvolved images. The benefit is that photon noise can be reduced by including more pixels.

4. DISCUSSION

Deconvolution is a useful tool for sharpening and increasing the contrast in retinal images because of the reduction or removal of extended PSF structure. We have demonstrated that deconvolution also improves quantitative measurements from retinal images, specifically individual cone reflectances. We applied an MFBD algorithm to the simulated and real data reported here because of the absence of any known PSF information. The simulated data analysis showed that the deconvolution and cone-reflectance measurement procedure can measure the absorptances to within 10% of the true values, which is suitable for determination of cone class. On application to previously analyzed macaque retinal images, the error in the L- and M-cone assignments is reduced by almost a factor of 2. The primary error in cone assignment is the residual blur with additional contributions due to noise in the data and the individual cone-reflectance variations. The latter is minimized by using interlaced data for the three different bleach states so that when the blur is removed, the primary error in the cone assignments is due to noise. This noise is reduced by increasing the number of images taken. The analysis presented here shows that with deconvolution we achieved an assignment error of 5% with 36% fewer images than without deconvolution.

It should be noted that nonphysical absorptance values were obtained after deconvolution. For example, after the 650- and 470-nm bleach, some cones showed negative absorptance. For that to happen, a partially bleached retina would have to reflect more light than a fully bleached one, which is not possible. Such results could arise if the "full bleach" were incomplete, but we do not expect this to be the case. More likely, the deconvolution was more effective at pulling light into the core of the cones for the partial-bleach conditions, to the extent that it exaggerated the contrast of the original object. Differences in the quality of the deconvolved images, e.g., the size of the reconstructed cones for the different bleach cases, can certainly contribute to this, especially with use of the same-size circular aperture for the measurements. For these data, negative absorptance is not a problem, since we were more concerned with distinguishing the

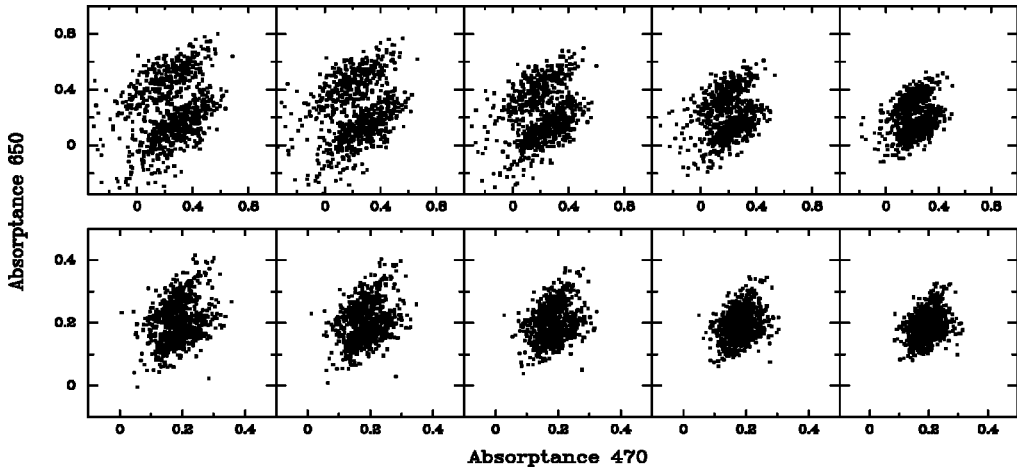

Fig. 9. Cone classification for L and M cones from the absorptance measurements for the averaged retinal images in Fig. 6 (bottom) compared with the corresponding deconvolved images in Fig. 7 (top). The differences due to the aperture size used for the measurements are shown for (from left to right) circular radii of 1.5, 2, 3, 4, and 5 pixels.

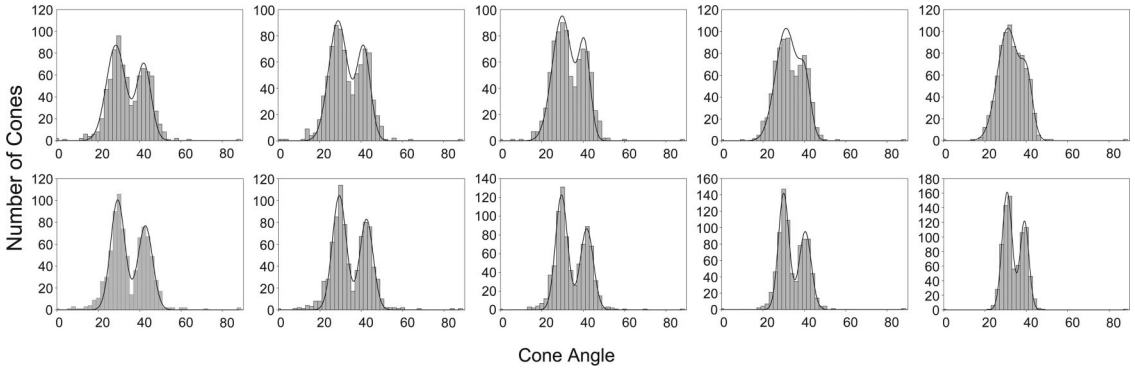

Fig. 10. Histograms and best fits of a double Gaussian to the distributions shown in Fig. 9 for circular aperture radii of (left to right) 1.5, 2, 3, 4, and 5 pixels with (bottom) and without (top) deconvolution.

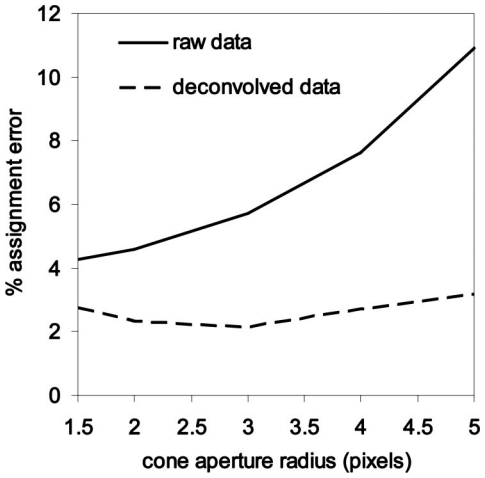

Fig. 11. Plot of percentage assignment error versus cone aperture radius in pixels. The smallest cone assignment error for the deconvolved images is 2.16%, which represents a nearly twofold improvement over the analysis of the raw images.

cones than with measuring their true shape or contrast. This is an example of how the end goals of the deconvolution process must be specified clearly and the constraints must be set accordingly. To obtain a good measure of the true shape of the cones, a good estimate of the PSF is needed, which was not available for these data. A good estimate of the PSF can be obtained from measurements of the residual wave-front errors that can be used in conjunction with the retinal images for deconvolution from wave-front sensing.[2–4] However, although the correction may be good, the retinal image may be degraded by unsensed aberrations such as tear film and retinal motion, and a myopic approach would be preferable.[21]

The success of the technique confirmed that the radiometry of the original cones, rather than the actual object, was retained after the deconvolution, which is not a feature of many deconvolution algorithms but was a constraint that was put on these results.

ACKNOWLEDGMENTS

This work has been supported by the National Science Foundation Science and Technology Center for Adaptive Optics, managed by the University of California at Santa Cruz under cooperative agreement AST-9876783. Some of the data analysis reported here used the IRAF package that is written and supported by the IRAF programming group at the National Optical Astronomy Observatories (NOAO) in Tucson, Arizona. NOAO is operated by the Association of Universities for Research in Astronomy (AURA), Inc., under cooperative agreement with the National Science Foundation.

Corresponding author Julian Christou's e-mail address is christou@ucolick.org.

REFERENCES

1. J. Liang, D. R. Williams, and D. Miller, "Supernormal vision and high-resolution retinal imaging through adaptive optics," J. Opt. Soc. Am. A **14**, 2884–2892 (1997).
2. I. Iglesias and P. Artal, "High-resolution images obtained by deconvolution from wavefront sensing," Opt. Lett. **25**, 1804–1806 (2000).
3. D. Catlin and C. Dainty, "High-resolution imaging of the human retina with a Fourier deconvolution technique," J. Opt. Soc. Am. A **19**, 1515–1523 (2002).
4. J. Arines and S. Bara, "Hybrid technique for high resolution imaging of the eye fundus," ACI Mater. J. **11**, 761–766 (2003); www.opticsexpress.org.
5. A. Roorda and D. R. Williams, "The arrangement of the three cone classes in the living human eye," Nature **397**, 520–522 (1999).
6. A. Roorda, A. B. Metha, P. Lennie, and D. R. Williams, "Packing arrangement of the three cone classes in primate retina," Vision Res. **41**, 1291–1306 (2001).
7. H. Hofer, L. Chen, G. Yoon, B. Singer, Y. Yamauchi, and D. R. Williams, "Improvement in retinal image quality with dynamic correction of the eye's aberrations," ACI Mater. J. **8**, 631–643 (2001); www.opticsexpress.org.
8. T. J. Holmes, R. J. Ramirrez, D. G. Bartsch, N. J. O'Conner, and W. R. Freeman, "Deconvolution and automatic alignment of indocyanine green fundus tomograms: initial study of feasibility," Invest. Ophthalmol. Visual Sci. Suppl. **37**, S608 (1996).
9. F. W. Campbell and W. A. H. Rushton, "Measurement of the scotopic pigment in the living human eye," J. Physiol. (London) **130**, 131–147 (1955).
10. W. A. H. Rushton and H. D. Baker, "Red/green sensitivity in normal vision," Vision Res. **4**, 75–85 (1964).
11. D. A. Baylor, B. J. Nunn and J. L. Schnapf, "Spectral sensitivity of cones of the monkey Macaca Fascicularis," J. Physiol. (London) **390**, 145–160 (1987).
12. G. Wyszecki and W. S. Stiles, "Theories and models of color vision," in *Color Science: Concepts and Methods, Quantitative Data and Formulae* 2nd ed. (Wiley, New York, 1982).
13. W. H. Richardson, "Bayesian-based iterative method of image restoration," J. Opt. Soc. Am. **62**, 55–59 (1972).
14. L. B. Lucy, "An iterative technique for the rectification of observed distributions," Astron. J. **79**, 745–754 (1974).
15. S. M. Jefferies and J. C. Christou, "Restoration of astronomical images by iterative blind deconvolution," Astrophys. J. **415**, 862–874 (1993).
16. J. C. Christou, D. Bonaccini, N. Ageorges, and F. Marchis, "Myopic deconvolution of adaptive optics images," ESO Messenger **97**, 14–22 (1999).
17. R. J. Hanisch and R. L. White, ed., *The Restoration of HST Images & Spectra II* NASA/Goddard Space Telescope Science Institute (NASA/Space Telescope Science Institute, Baltimore, Md., 1994).
18. D. Barnaby, E. Spillar, J. C. Christou, and J. D. Drummond, "Measurements of binary stars with the Starfire Optical Range Adaptive Optics Systems," Astron. J. **119**, 378–389 (2000).
19. J. C. Christou, G. Pugliese, R. Koehler, and J. D. Drummond, "Photometric and astrometric analysis of Gemini Galactic Center observations using 'StarFinder' and blind deconvolution packages," Bull. Am. Astron. Soc. **34**, 1202 (2003).
20. A. Pallikaris, D. R. Williams, and H. Hofer, "The reflectance of single cones in the living human eye," Invest. Ophthalmol. Visual Sci. **44**, 4580–4592 (2003).
21. L. Mugnier, C. Robert, J.-M. Conan, V. Michau, and S. Salem, "Myopic deconvolution from wave-front sensing," J. Opt. Soc. Am. A **18**, 862–872 (2001).